nature materials

LETTERS

https://doi.org/10.1038/s41563-018-0107-4

Homochiral porous nanosheets for enantiomer sieving

Bo Sun[1], Yongju Kim[1]*, Yanqiu Wang[1], Huaxin Wang[1], Jehan Kim[2], Xin Liu[1] and Myongsoo Lee[1]*

Protein pores are highly specific in binding to chiral substrates and in catalysing stereospecific reactions, because their active pockets are asymmetric and stereoselective[1,2]. Chiral binding materials from molecular-level pores with high specificity have not been achieved because of problems with pore deformation and blocking[3]. A promising solution is the self-assembly of single sheets where all pores are exposed to the environment, for example as metal–organic frameworks[4], polymers[5,6] or non-covalent aromatic networks[7–10], but, typically, the pores are distant from the internal cavities with chirality. Here, we report the synthesis of homochiral porous nanosheets achieved by the 2D self-assembly of non-chiral macrocycles, with open/closed pore switching. Pore chirality is spontaneously induced by a twisted stack of dimeric macrocycles. The porous 2D structures can serve as enantiomer sieving membranes that exclusively capture a single enantiomer in a racemic mixture solution, with uptake capacity greater than 96%. Moreover, the entrapped guests inside the pores can be pumped out by pore closing triggered by external stimuli. This strategy could provide new opportunities for controlled molecule release, as well as for artificial cells.

Aromatic macrocycles are intrinsically porous structures[11–16], so they are ideal candidates for the construction of porous materials with uniform pore size by self-assembly into an extended nanostructure. When stacking two macrocycles, the twist between two macrocycles breaks mirror symmetry, leading to a chiral cavity[17]. We envision that such a stacked macrocycle dimer could be utilized as a self-assembling subunit for homochiral porous nanosheets that replicate the specific chiral recognition of individual pore subunits.

Here, the molecule that forms a chiral pore through dimeric stacking consists of an aromatic macrocycle and a chiral oligoether dendron at the centre of the macrocycle plane to inhibit continuous aromatic stacking in one dimension (Fig. 1a). Molecule **1** (Supplementary Figs. 1–3) self-assembles into dimeric micelles, which, in turn, grow in two dimensions in methanol to form flat sheet structures (Fig. 1b). Cryogenic transmission electron microscopy (cryo-TEM) of the structures showed isolated sheet objects with straight edges, ranging in their lateral dimensions from submicrometre to several micrometres, indicating that the sheets are robust and free-standing in bulk solution (Fig. 2a). To obtain more information about the sheets, TEM experiments were also performed with cast films. These revealed flat 2D structures, consistent with the cryo-TEM results (Fig. 2b). A high-resolution image obtained from aged solution revealed uniform nanosized aggregates with a diameter of 1.9 nm, arranged in short-range 2D hexagonal order (Fig. 2c and Supplementary Fig. 4). This was further confirmed by selected area electron diffraction, which showed diffuse ring patterns with three concentric rings of maximum intensity, indicative of a slightly broad spatial distribution of the centres of the primary aggregates (Fig. 2d). Assuming 2D hexagonal order, the primary *d* spacing indicates an inter-aggregate distance of 1.96 nm, which is consistent with the micellar size. Atomic force microscopy (AFM) analysis showed that the sheets are very flat and uniform with a thickness of 2.8 nm (Fig. 2e and Supplementary Fig. 5). Considering the molecular size of **1**, this thickness, together with the lateral dimension obtained from TEM, suggests that the primary structure consists of two molecules in which the aromatic macrocycles face one another. This was further confirmed by topochemical polymerization of the sheet solution, which exclusively produced dimers with a lack of any higher-molecular-weight fractions (Supplementary Fig. 6). Taking all the data together, we propose that the primary micelles consist of stacked dimers that are laterally associated into a 2D superstructure to form free-standing sheets (Supplementary Fig. 7).

When diluted, TEM showed the formation of well-separated discrete micelles that subsequently assemble laterally into planar structures at higher concentrations (Fig. 3a–c). This demonstrates that discrete micelles formed at earlier stages of the self-assembly propagate only in two dimensions, prohibiting 3D growth[15]. This result suggests that the dendrimer-grafted macrocycles face one another to form a paired dimer with opposing dendritic chains at the aromatic basal planes. The dimeric micelles in turn grow laterally through side-to-side solvophobic interactions to form 2D sheets (Fig. 1b). Calculation showed that the aromatic plane adopts a saddle-shaped conformation with the dendrimer located at the opposite basal plane to the protruded apex phenylenes to reduce the steric hindrance between the adjacent *ortho*-hydrogens in the *meta*-terphenyl linkage of the macrocycle (Fig. 3d). To maximize aromatic interactions between the faced macrocycles with a nonplanar conformation, the paired aromatic segments are rotationally offset from each other with a twist angle of 60°, as confirmed by rotating frame nuclear Overhauser effect (ROE) measurements (Fig. 3e and Supplementary Figs. 3, 8 and 9). The twisted stacking of the aromatic segments is also reflected in a redshifted absorption maximum and fluorescence enhancement in methanol solution compared to measurements in chloroform (Fig. 2f)[18].

Another important aspect to be considered is the ability to twist in a preferred rotation due to chirality transfer from the chiral oligoether dendron to the achiral macrocycle. According to the same symmetry-breaking principle[19], the twisted stacking of the two macrocycles in a preferred rotation would generate a dimeric superstructure with a chiral cavity. Indeed, the methanol solution of **1*S*** revealed a strong circular dichroism (CD) signal (Fig. 3f and Supplementary Fig. 10), demonstrating that the stacked macrocycle dimers adopt the twisted conformation with a preferred rotation, giving rise to a chiral superstructure. Assemblies derived from the

[1]State Key Laboratory of Supramolecular Structure and Materials, College of Chemistry, Jilin University, Changchun, China. [2]Pohang Accelerator Laboratory, Postech, Pohang, Gyeongbuk, Korea. *e-mail: yjkim@jlu.edu.cn; mslee@jlu.edu.cn

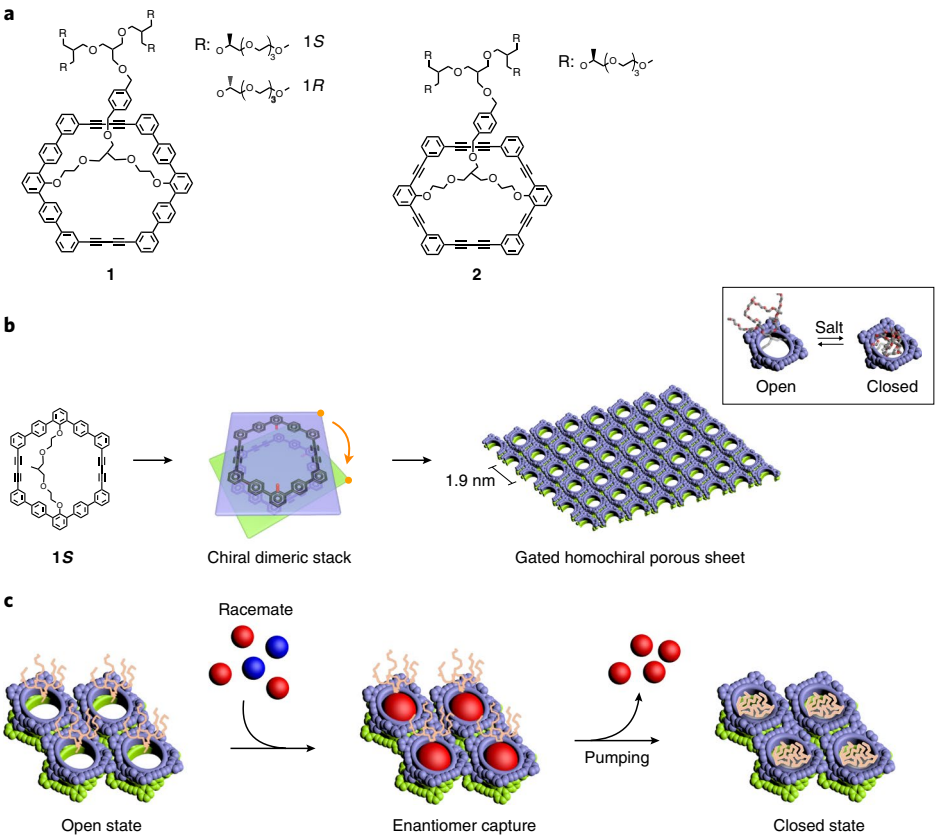

Fig. 1 | Self-assembly of dimeric chiral pores into a gated homochiral porous nanosheet. a, Molecular structure of aromatic macrocycles **1** and **2**. **b**, Schematic representation for the formation of a homochiral porous nanosheet through lateral assembly of the twist dimeric macrocycle stack. The pores are alternately open and closed in response to salt. **c**, Chiral recognition, enantioselective uptake of a racemate guest and pumping of the entrapped guest by addition of salt from the enantiomer sieving sheet.

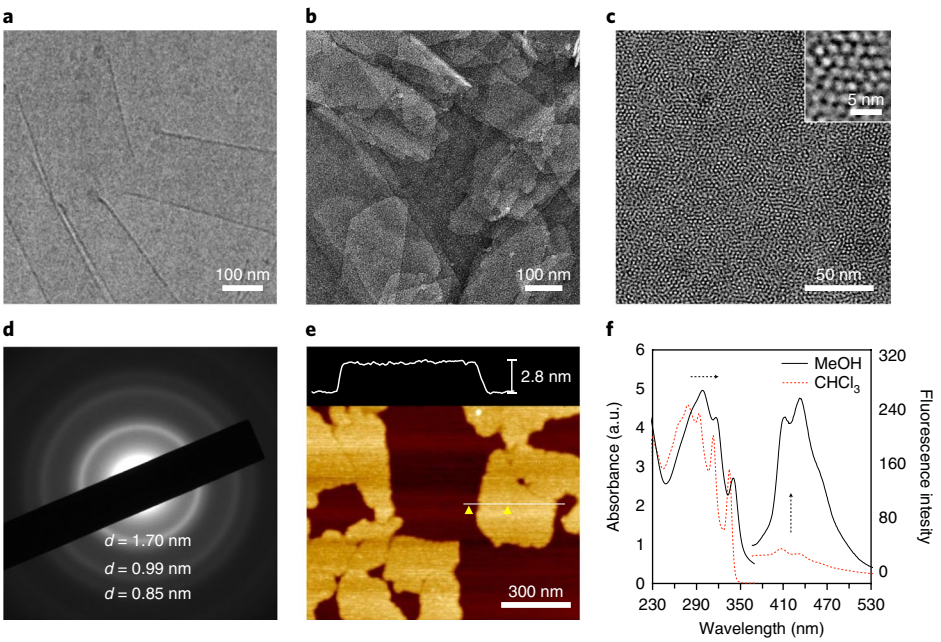

Fig. 2 | Structural characterization of homochiral porous nanosheets. a,**b**, Cryo-TEM image (**a**) and negatively stained TEM image (**b**) of **1*S*** (45 μM) in methanol. **c**, High-resolution TEM image obtained after one week ageing of **1*S*** (45 μM) in methanol. Inset: magnified image showing short-range 2D hexagonal order. **d**, Selected area electron diffraction pattern includes three rings measured at 1.70, 0.99 and 0.85 nm. **e**, AFM height image of sheets on mica. The sample film was dropcast from **1*S*** (45 μM) in methanol solution after five days of ageing. The cross-sectional profile (top) is taken along the white line. **f**, Absorption and emission spectra (excitation wavelength, 293 nm) of **1*S*** (45 μM) in methanol (black solid line) and in chloroform solution (red dashed line).

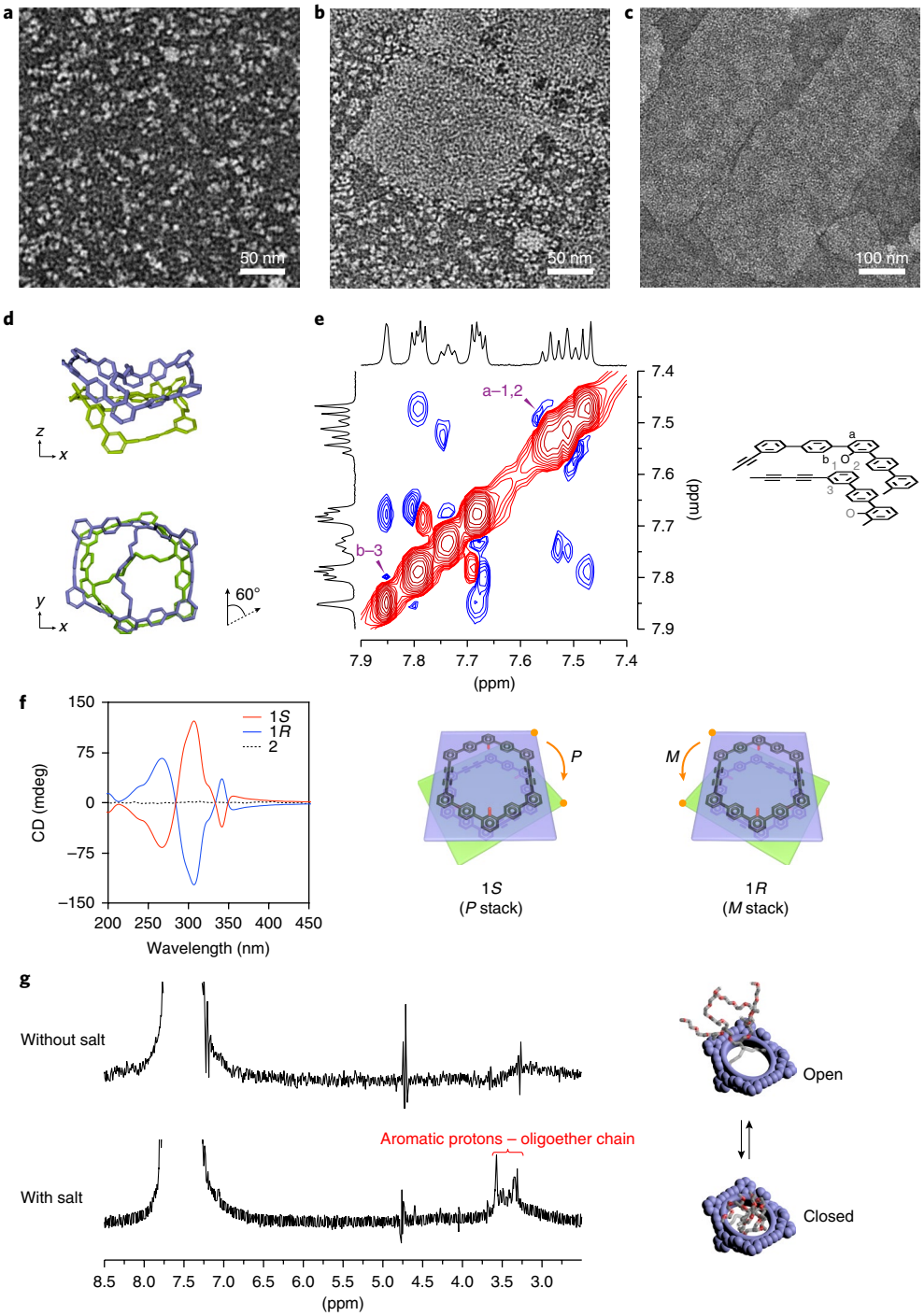

Fig. 3 | Two-dimensional growth of chiral pores and gating behaviour. a–c, Negatively stained TEM images of 4.5 μM (**a**), 22.5 μM (**b**) and 45 μM (**c**) of **1S** in methanol. **d**, Energy minimization of the dimeric macrocycle, demonstrating paired aromatic segments with a twist angle of 60°. **e**, 2D ROE spectrum from **1S** (712 μM) in methanol-d_4/THF-d_8 (4:1, vol/vol). The correlations of a–1,2 and b–3 indicate the twisted stacking of the aromatic segments with a rotational angle of approximately 60°, which are not observed in chloroform solution (Supplementary Fig. 3). **f**, CD spectra of **1S** (red solid line), **1*R*** (blue solid line) and **2** (black dashed line) in methanol solution (45 μM), and schematic representation of twist stacking of dimeric macrocycles. The twist directions of **1S** (*P* stack) and **1*R*** (*M* stack) were determined from the experimental results and calculation data based on interactions between chiral pore and guest molecules in Fig. 4c. **g**, 1D NOE spectra of **1S** (712 μM) in methanol-d_4/THF-d_8 (4:1, vol/vol) without and with ammonium acetate salt (40 mM). Irradiation at 7.45–7.54 ppm (corresponding to proton a, 1 and 2 in **e**) with salt-induced NOE correlations with oligoether chains at 3.28–3.60 ppm, indicative of the collapse of oligoether chains onto the macrocycles, causing the open pores to be closed.

enantiomer of **1*R*** exhibit opposite CD signal with a perfect mirror image relationship, indicating that the chirality of the dendron is transferred to the self-assembly of the macrocycles to form homochiral nanoporous structures (Supplementary Figs. 11–13). These results indicate that the macrocycle adopts a non-planar, saddle-shaped conformation that drives the stacked dimers to be

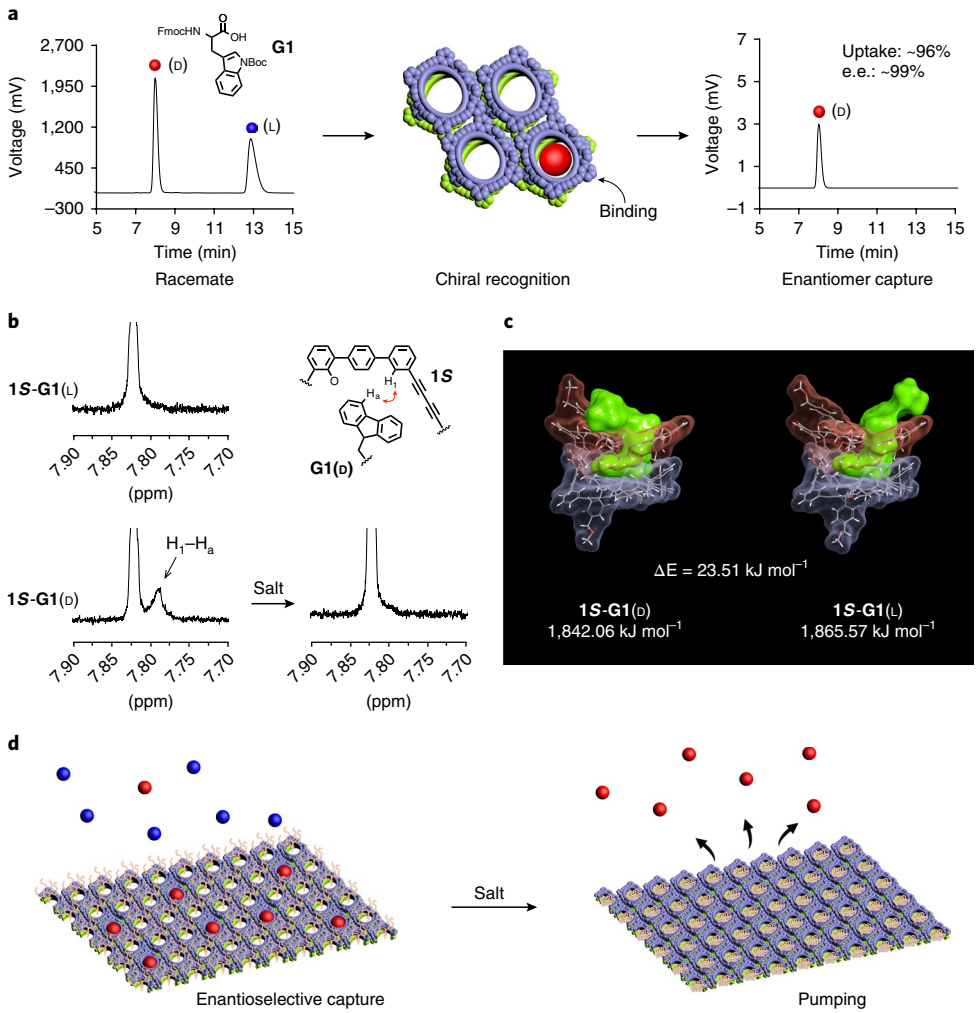

Fig. 4 | Enantiomer sieving and pumping action. a, Chiral recognition and macroscopic separation. HPLC spectra of a racemic tryptophan derivative (left) and exclusive uptake of the D form (right) by **1S** sheet in methanol solution. **b**, 1D NOE spectra from **1S** (712 μM)-**G1(L)** (356 μM) and **1S** (712 μM)-**G1(D)** (356 μM) in methanol-d_4/THF-d_8 (4:1, vol/vol). Ammonium acetate (40 mM) was added to **1S**-**G1(D)**. Irradiation at 7.82 ppm (H_1 peak) induced an NOE peak at 7.79 ppm in **1S**-**G1(d)** solution before the addition of salt, indicative of coupling between the macrocycle interior (H_1) and the fluorenyl group (H_a) of the D form. **c**, MD simulations for the calculation of energies between *P*-stacked chiral pore-**G1(D)** and *P*-stacked chiral pore-**G1(L)**. **d**, Schematic representation of the responsive homochiral porous nanosheet for a 2D enantiomer sieve with molecular pumping.

arranged in a staggered order to fit into one another with rotational restriction, generating a chiral dimeric superstructure and homochiral porous sheets (Fig. 1b).

To further understand the structural requirements needed to form twisted chiral pores, analogue **2** was synthesized (Supplementary Figs. 1 and 14) and studied in terms of chiral-forming capability (Fig. 3f). From control experiments with **2**, which adopts a more planar conformation (Supplementary Figs. 15–17), it can be considered that a saddle-like and non-planar conformation of aromatic macrocycle is essential to form chiral pores in stacked macrocycle dimers.

Notably, the chiral pores can be closed by the addition of salts because the oligoether chains can be desolvated to collapse into the macrocycles[20]. Indeed, following the addition of ammonium acetate, the ^{1}H NMR resonances associated with the ethyleneoxide chains of **1** are decreased in intensity (Supplementary Fig. 18), indicative of desolvation of the oligoether chains[21]. Moreover, 1D NOE correlations between the aromatic segment and the oligoether chains are induced with the addition of salt, demonstrating collapse of the oligoether chains into the macrocycle cavities, closing the pores (Fig. 3g and Supplementary Fig. 19).

The gated chiral pores preferentially bind one enantiomer over the other in the open state[22–24]. To explore the capability of the homochiral porous sheets for single enantiomer capture in racemic solution, hydrophobically protected tryptophan (**G1**) was selected because the pores consist of a hydrophobic, aromatic interior compatible with the guest size (Fig. 4a). We found that the pores show greater than 96% uptake of the tryptophan guest (Supplementary Figs. 20–22), indicating that guest uptake is nearly perfect. This provides evidence that the 2D sheet structure preserves subunit porosity without compromising the pore performance for guest uptake, unlike 3D chiral porous materials[25]. It is worth noting that the CD signal of the sheets remains unchanged even after inclusion of the enantiomer guests, indicating that the dimeric macrocycle with a chiral cavity retains a fixed conformation, even with guest inclusion (Supplementary Fig. 23).

The preferential capture of enantiomers by the porous sheets was monitored by tracing chiral HPLC. The obtained profile shows the peak associated with the D enantiomer of the tryptophane guest, but no noticeable trace associated with the L enantiomer (Fig. 4a), demonstrating that the porous sheets of **1S**

exclusively take up the D form, with perfect inclusion preference over the L form (Fig. 1c and Supplementary Figs. 24–27). These results support the conclusion that the dimeric macrocycle pores in the sheets are homochiral. Consistent with the separation results, NOE measurements showed a prominent peak at 7.79 ppm associated with the strong coupling between H_i of the macrocycle interior and H_a of the fluorenyl group in the D form, in sharp contrast to the L form, which lacks this in the NOE signal (Fig. 4b and Supplementary Fig. 28). This coupling was further confirmed by fluorescence enhancement at 411 nm on trapping the guests, which could be attributed to the restricted rotation of the phenyl groups on the aromatic backbone (Supplementary Fig. 22)[26]. Molecular dynamics (MD) calculations showed that the fluorenyl group of the D form in **1*S*** occupies the macrocycle cavity, while both indole and *tert*-butyl groups are in close proximity to the benzyl linker (Fig. 4c and Supplementary Fig. 29). In contrast, the indole group of the L enantiomer is located out of the benzyl group, indicative of geometric mismatch with the chiral interior. This leads to a large difference in calculated binding energy between the D and L forms in **1*S*** of approximately 23.5 kJ mol^{-1}, which explains the observed enantioselectivity. Meanwhile, the **1*R*** sheets exclusively take up the opposite enantiomer (Supplementary Figs. 20 and 30), providing strong evidence for the handedness of the enantiopure dimeric macrocycle cavity (Supplementary Fig. 31).

To substantiate the gating behaviour of the pores, binding experiments with **1*S*** were performed with the D enantiomer of **G1** in the presence of ammonium acetate (40 mM). Unlike in salt-free solution, HPLC and fluorescence measurements indicate that the sheets are unable to entrap the guests, showing that the chiral pores in the presence of the salt are blocked by shrinking of the oligoether chains for guest binding (Supplementary Fig. 32). Remarkably, when the pores entrap the enantiomer, closing of the pores is accompanied by pumping of the entrapped guests out of the pores. With addition of the salt to the enantiomer-entrapped nanosheet solution, the enhanced fluorescence emission at 411 nm returns back to the guest-free state (Supplementary Fig. 33) and the NOE signal associated with the cavity–guest interactions disappears to also recover the guest-free state (Fig. 4b). These results demonstrate that the entrapped guests inside the pores are pumped out by shrinking of the oligoether chains inside the cavities, triggered by the addition of salt (Figs. 1c and 4d).

To evaluate the uptake capacity and enantioselectivity of the sheets with different amino acid derivatives, we carried out the same experiments with Fmoc- and *tert*-butyl-protected tyrosine (**G2**) (Supplementary Figs. 20 and 34). Similar to the tryptophan derivative **G1**, enantioselectivity in the tyrosine derivative was found to be nearly perfect, with high uptake capacity (>94% occupied pores). In sharp contrast, the sheets do not exhibit any apparent inclusion activity for smaller Fmoc-protected amino acids such as phenylalanine (**G3**), alanine (**G4**) and leucine (**G5**). The clearcut selectivity in both size and chirality, as well as the nearly perfect uptake capacity, are believed to be attributed to successful translation of accurate molecular recognition of individual chiral pores into the extended nanostructure without sacrificing pore performance.

As a result, our approach can contribute to the spontaneous formation of highly efficient enantiomer sieving membranes, which selectively adsorb enantiomers with only one discrimination event, either binding or non-binding (Supplementary Fig. 27). This is in contrast to 3D chiral porous materials, which rely on a series of interactions between the racemate and pore walls[26]. This capability of enantioseparation in a single molecular event could allow our 2D materials to become a highly efficient alternative to current separation methods. We believe that our strategy will provide additional opportunities to construct gated plasma membranes, nanopumps and multiple copies of artificial intracellular machines.

Methods

Methods, including statements of data availability and any associated accession codes and references, are available at https://doi.org/10.1038/s41563-018-0107-4.

Received: 30 June 2017; Accepted: 11 May 2018;
Published online: 11 June 2018

References

1. Gilson, M. K. & Zhou, H.-X. Calculation of protein–ligand binding affinities. *Annu. Rev. Biophys. Biomol. Struct.* **36**, 21–42 (2007).
2. Stank, A., Kokh, D. B., Fuller, J. C. & Wade, R. C. Protein binding pocket dynamics. *Acc. Chem. Res.* **49**, 809–815 (2016).
3. Cui, Y. et al. Metal–organic frameworks as platforms for functional materials. *Acc. Chem. Res.* **49**, 483–493 (2016).
4. Peng, Y. et al. Metal–organic framework nanosheets as building blocks for molecular sieving membranes. *Science* **346**, 1356–1359 (2014).
5. Kissel, P. et al. A two-dimensional polymer prepared by organic synthesis. *Nat. Chem.* **4**, 287–291 (2012).
6. Kissel, P., Murray, D. J., Wulftange, W. J., Catalano, V. J. & King, B. T. A nanoporous two-dimensional polymer by single-crystal-to-single-crystal photopolymerization. *Nat. Chem.* **6**, 774–778 (2014).
7. Colson, J. W. et al. Oriented 2D covalent organic framework thin films on single-layer graphene. *Science* **332**, 228–231 (2011).
8. Dong, R. et al. Large-area, free-standing, two-dimensional supramolecular polymer single-layer sheets for highly efficient electrocatalytic hydrogen evolution. *Angew. Chem. Int. Ed.* **54**, 12058–12063 (2015).
9. Zhang, K. D. et al. Toward a single-layer two-dimensional honeycomb supramolecular organic framework in water. *J. Am. Chem. Soc.* **135**, 17913–17918 (2013).
10. Yue, L. et al. Flexible single-layer ionic organic–inorganic frameworks towards precise nano-size separation. *Nat. Commun.* **7**, 10742 (2016).
11. Iyoda, M. & Shimizu, H. Multifunctional π-expanded oligothiophene macrocycles. *Chem. Soc. Rev.* **44**, 6411–6424 (2015).
12. Huang, Z. et al. Pulsating tubules from noncovalent macrocycles. *Science* **337**, 1521–1526 (2012).
13. Percec, V. et al. Self-assembly of amphiphilic dendritic dipeptides into helical pores. *Nature* **430**, 764–768 (2004).
14. Colson, J. W. & Dichtel, W. R. Rationally synthesized two-dimensional polymers. *Nat. Chem.* **5**, 453–465 (2013).
15. Kim, Y. et al. Switchable nanoporous sheets by the aqueous self-assembly of aromatic macrobicycles. *Angew. Chem. Int. Ed.* **52**, 6426–6429 (2013).
16. Shimizu, H. et al. Synthesis, structures, and photophysical properties of π-expanded oligothiophene 8-mers and their Saturn-like C_{60} complexes. *J. Am. Chem. Soc.* **137**, 3877–3885 (2015).
17. Lee, S., Chen, C.-H. & Flood, A. H. A pentagonal cyanostar macrocycle with cyanostilbene CH donors binds anions and forms dialkylphosphate [3] rotaxanes. *Nat. Chem.* **5**, 704–710 (2013).
18. Würthner, F., Kaiser, T. E. & Saha-Möller, C. R. J-aggregates: from serendipitous discovery to supramolecular engineering of functional dye materials. *Angew. Chem. Int. Ed.* **50**, 3376–3410 (2011).
19. Wang, Y., Xu, J., Wang, Y. & Chen, H. Emerging chirality in nanoscience. *Chem. Soc. Rev.* **42**, 2930–2962 (2013).
20. Huang, K. & Szleifer, I. Design of multifunctional nanogate in response to multiple external stimuli using amphiphilic diblock copolymer. *J. Am. Chem. Soc.* **139**, 6422–6430 (2017).
21. Nelson, J. C., Saven, J. G., Moore, J. S. & Wolynes, P. G. Solvophobically driven folding of nonbiological oligomers. *Science* **277**, 1793–1796 (1997).
22. Chen, L. et al. Separation of rare gases and chiral molecules by selective binding in porous organic cages. *Nat. Mater.* **13**, 954–960 (2014).
23. Zhang, G.-W. et al. Triptycene-based chiral macrocyclic hosts for highly enantioselective recognition of chiral guests containing a trimethylamino group. *Angew. Chem. Int. Ed.* **55**, 5304–5308 (2016).
24. Hauser, A. W. et al. Functionalized graphene as a gatekeeper for chiral molecules: an alternative concept for chiral separation. *Angew. Chem. Int. Ed.* **53**, 9957–9960 (2014).
25. Seo, J. S. et al. A homochiral metal–organic porous material for enantioselective separation and catalysis. *Nature* **404**, 982–986 (2000).
26. Xie, R., Chu, L.-Y. & Deng, J.-G. Membranes and membrane processes for chiral resolution. *Chem. Soc. Rev.* **37**, 1243–1263 (2008).

Acknowledgements

This work was supported by the National Natural Science Foundation of China (grants 21634005, 51473062 and 21574055) and Jilin University Funding (JLUSTIRT).

Author contributions

B.S. synthesized molecules, measured spectroscopic data, carried out the uptake experiments. Y.K. performed chiral separation and molecular simulations, and

supervised the research. Y.W. performed TEM experiments. H.W. carried out NMR experiments. J.K. performed X-ray experiments. X.L. measured electron diffraction. M.L. developed the concept, supervised the research and wrote the manuscript with input from all authors.

Competing interests

The authors declare no competing interests.

Additional information

Supplementary information is available for this paper at https://doi.org/10.1038/s41563-018-0107-4.

Correspondence and requests for materials should be addressed to Y.K. or M.L.

Methods

General. The morphology of the homochiral porous sheet was characterized by TEM and AFM according to the procedures reported in ref. [27]. All reactions were performed in oven-dried glassware under a dry argon atmosphere. Toluene and tetrahydrofuran (THF) were dried by distillation from sodium benzophenone immediately before use. Dichloromethane (DCM) was dried by distillation from CaH_2. Distilled water was prepared by ion exchange and filtration. Other solvents and organic reagents were purchased from commercial vendors and used without further purification unless otherwise mentioned. The products were purified by flash column chromatography on silica gel (230–400 mesh). Thin-layer chromatography was performed on precoated glass-backed plates (silica gel 60 F_{254} 0.25 nm), and components were visualized by observation under ultraviolet light (254 and 365 nm) or by treating the plates with iodine, anisaldehyde, $KMnO_4$, phosphomolybdic acid and vanillin followed by heating. ^{1}H and ^{13}C NMR spectra were obtained on 600, 500 or 300 MHz Fourier transform (FT) NMR spectrometers. All compounds were subjected to ^{1}H NMR analysis to confirm ≥98% sample purity. Chemical shifts were reported in ppm relative to the residual solvent peak ($CDCl_3$:^{1}H, 7.26; ^{13}C, 77.23) or tetramethylsilane (TMS) peak. Multiplicity was indicated as follows: s (singlet), d (doublet), t (triplet), m (multiplet), dd (doublet of doublets). Coupling constants are reported in Hz. Matrix-assisted laser desorption/ionization time of flight mass spectrometry (MALDI-TOF MS) was performed on a Bruker Autoflex TOF/TOF using *trans*-2-[3-(4-*tert*-butylphenyl)-2-methyl-2-propenylidene]malononitrile as a matrix. UV–vis, fluorescence and CD spectra were obtained using a Hitachi U-2900 spectrophotometer, Hitachi F-7000 fluorescence spectrophotometer and Jasco J-810 spectropolarimeter, respectively. X-ray scattering measurements were performed in transmission mode with synchrotron radiation at the 3C X-ray beamline at Pohang Accelerator Laboratory, Korea. Analytic and preparatory HPLC were performed with a Prominence LC-20AP (Shimadzu) using a YMC C4 reverse-phase column (250 × 4.6 mm ID S-5 μm, 12 nm) for the quantification of uptake and a YMC Chiral ART Cellulose-C column (250 × 4.6 mm ID S-5 μm) for the chiral separation.

TEM experiments. To investigate the self-assembled structures, a drop of the sample solution of macrocyles (0.001–0.01 wt%) was placed on a carbon-coated copper grid (carbon type B (15–25 nm) on 200 mesh with Formvar, Ted Pella), and the solvent was allowed to evaporate under ambient conditions. The samples were then stained by depositing a drop of uranyl acetate aqueous solution (0.2–1.0 wt%) onto the surface of the sample-loaded grid. The dried specimens were observed using a JEOL-JEM HR2100 instrument operating at 120 kV. Cryo-TEM experiments were performed with a thin film of the sample solution of macrocycles (5 μl) transferred to a locally supported grid at room temperature (lacey formvar/carbon, 200 mesh, Cu, Ted Pella). The thin solution films were prepared under controlled temperature and humidity conditions in a custom-built environmental chamber to prevent evaporation of methanol from the sample solution. Excess liquid was blotted with filter paper for 2–3 s, and the thin solution films were rapidly vitrified by plunging them into liquid ethane (cooled by liquid nitrogen) at its freezing point. The grid was transferred onto a Gatan 626 cryoholder using a cryo-transfer device and transferred to a JEM HR2100 TEM. Direct imaging was carried out at a temperature of approximately –175 °C and with 120 kV accelerating voltage, using the images acquired with a Dual Vision 300 W and SC 1000 charge-coupled device camera (Gatan). Data were analysed using Digital Micrograph software.

AFM experiments. The sample film on a mica surface was prepared by dropcasting **1*S*** (45 μM) in methanol solution after 5 days of ageing. The measurements were conducted on a MultiMode 8 AFM with NanoScope V controller, NanoScope software and NanoScope Analysis software (Bruker AXS Corporation) in air at ambient temperature (~25 °C). Images were acquired in peak force tapping mode.

Molecular simulations. The energies of the dimeric macrocycle with twist angles of 0 and 60° were calculated using the Material Studio 6.0 program (Accelrys Software) to evaluate relative stability. Truncated structures were used to reduce the calculation time. The preliminary geometry of the molecules was optimized using Forcite module with universal force field (UFF). Fine geometry optimizations were then performed with the DMol^3 module based on density functional theory (DFT) with the following parameters—spin polarization: restricted; charge: 0; basis: dnp; pseudopotential: none; functional: pbe; aux density: octupole; integration grid: medium; occupation: fermi; cutoff global: 3.30 Å; scf density convergence: 1.00e-5; scf charge mixing: 0.200; scf iterations: 50; scf diis: 6 pulay.

The total energies of the twisted dimeric macrocycle and **G1** (D or L) were simulated with MD using the MacroModel module from Schrödinger Suites (Schrödinger) with the following parameters—force field: OPLS3; solvent: MeOH (ε 32.7); cutoff: none; minimization method: PRCG; maximum iterations: 2,500; converge on: gradient; convergence threshold: 0.05; dynamics method: stochastic dynamics; simulation temperature: 300.0 K; time step: 1.5 fs; equilibrium time: 1.0 ps; simulation time: 10,000 ps. The dynamics of chiral pore and guest were performed under the constrained positions of the twisted aromatic segments.

To investigate the direction of the twisted packing in the dimer induced by the chiral dendron, all atomic simulations were performed with the MacroModel module in Schrödinger Suites with the above parameters. Four *M*-stack aromatic segments were arrayed and optimized into a hexagonal order. Full structures of the *S* or *R* dendrons were then introduced into the arrayed four *M*-stack dimers. The total energy and surface-area-to-volume ratio of four dimers with eight dendrons were compared on the constrained positions of *M*-stack aromatic segments via MD simulations.

NMR experiments. The twisted stacking of the dimeric macrocycle was confirmed by 2D ROE experiments. **1*S*** (712 μM) in methanol-d_4/THF-d_8 (4:1, vol/vol) was sonicated for 30 min. The sample solution was kept for 4 h at room temperature for stabilization, before 2D ROE spectra were measured on a 600 MHz FT NMR spectrometer. Interactions between the homochiral porous sheet and guest were confirmed by 1D nuclear Overhauser effect (NOE) experiments: 712 μM **1*S*** and 356 μM **G1**(D), and 712 μM **1*S*** and 356 μM **G1**(L) were prepared in methanol-d_4/THF-d_8 (4:1, vol/vol) with sonication for 30 min and stabilized for 4 h, then subjected to 1D NOE experiments on the 600 MHz FT NMR spectrometer. For experiments under salt conditions, ammonium acetate (20 and 40 mM) was added to **1*S*** (712 μM) in methanol-d_4, and the sample solutions were sonicated for 30 min and kept for 4 h at room temperature. Sample solutions were then measured using ^{1}H NMR spectra. 1D NOE correlations between the aromatic segment and the oligoether chains were obtained with **1*S*** (712 μM) with ammonium acetate (40 mM) in methanol-d_4/THF-d_8 (4:1, vol/vol). For the pumping study of guest binding in salt solution, 712 μM **1*S*** and 356 μM **G1**(D) in methanol-d_4/THF-d_8 (4:1, vol/vol) was prepared as described above, and 40 mM ammonium acetate was added to the sample solution. The mixture was sonicated for 30 min then kept for 4 h, and subjected to 1D NOE under irradiation at 7.82 ppm.

Uptake and chiral separation experiment. A 0.05 ml volume of a racemic mixture (**G1**–**G5**) in methanol solution (19.0 mM) was added to 0.45 ml of **1** methanol solution (274 μM) to a final concentration of **1** of 247 μM and an excess amount of the guest racemic mixture (1.9 mM). For stoichiometric experiments, sample solutions with 99 μM (0.4 equiv.), 198 μM (0.8 equiv.) and 296 μM (1.2 equiv.) of racemic mixture **G1** based on 247 μM **1*S*** in methanol were prepared. The samples were sonicated for 30 min and stabilized for 1 h at room temperature. After 1 h, the samples (0.2 ml) were run through a Sephadex LH-20 column to remove untrapped guest molecules. For measurements of uptake time of guest to pores, sample solutions (0.5 ml) of **1*S*** (247 μM) with **G1**(D) (0.95 mM) were sonicated for different time: 3, 6, 9, 12, 18, 24, 30, 45 and 60 min. The samples (0.2 ml) were then subjected immediately to a Sephadex LH-20 column. Sixteen fractions of 5.6 ml eluate (each 0.35 ml) were collected and concentrated under reduced pressure. Concentrated fractions were monitored by HPLC analysis. The uptake of guest into chiral pores was measured with a C4 column (250 × 4.6 mm ID S-5 μm) (CH_3CN with 0.1% formic acid; flow rate, 0.7 ml min^{-1}) and the enantiomeric excess of the captured guest was measured using a YMC Chiral ART Cellulose-C column (250 × 4.6 mm ID S-5 μm) under 15% EtOH in hexane (0.1% TFA; flow rate, 1.0 ml min^{-1}).

Topochemical polymerization. 1*S* (45 μM, 0.5 ml) in methanol was transferred to an ultraviolet quartz cuvette, then sealed with a screw cap. Polymerization was conducted under 254 nm ultraviolet light exposure and monitored by MALDI–TOF mass spectrometry and thin-layer chromatography every 5 min until the monomer was completely consumed.

Data availability. The data that support the findings of this study are available from the corresponding author upon reasonable request.

References

27. Kim, Y. et al. Open–closed switching of synthetic tubular pores. *Nat. Commun.* **6**, 8650 (2015).